ACS APPLIED MATERIALS & INTERFACES

Research Article

www.acsami.org

Influence of g-C_3N_4 Nanosheets on Thermal Stability and Mechanical Properties of Biopolymer Electrolyte Nanocomposite Films: A Novel Investigation

Yongqian Shi,[†,‡] Saihua Jiang,[†,‡] Keqing Zhou,[†] Chenlu Bao,[§] Bin Yu,[†,‡] Xiaodong Qian,[†,‡] Bibo Wang,[†] Ningning Hong,[†] Panyue Wen,[†,‡] Zhou Gui,*[,†] Yuan Hu,*[,†,‡] and Richard K. K. Yuen[‡,∥]

[†]State Key Laboratory of Fire Science, University of Science and Technology of China, 96 Jinzhai Road, Hefei, Anhui 230026, P. R. China

[‡]USTC-CityU Joint Advanced Research Centre, Suzhou Key Laboratory of Urban Public Safety, Suzhou Institute for Advanced Study, University of Science and Technology of China, 166 Ren'ai Road, Suzhou, Jiangsu 215123, P. R. China

[§]Department of Chemistry, National University of Singapore, 3 Science Drive 3, Singapore 117543, Singapore

[∥]Department of Building and Construction, City University of Hong Kong, Tat Chee Avenue, Kowloon, Hong Kong

Supporting Information

ABSTRACT: A series of sodium alginate (SA) nanocomposite films with different loading levels of graphitic-like carbon nitride (g-C_3N_4) were fabricated via the casting technique. The structure and morphology of nanocomposite films were investigated by X-ray powder diffraction, Fourier transform infrared spectroscopy, scanning electron microscopy, and transmission electron microscopy. Thermogravimetric analysis results suggested that thermal stability of all the nanocomposite films was enhanced significantly, including initial thermal degradation temperature increased by 29.1 °C and half thermal degradation temperature improved by 118.2 °C. Mechanical properties characterized by tensile testing and dynamic mechanical analysis measurements were also reinforced remarkably. With addition of 6.0 wt % g-C_3N_4, the tensile strength of SA nanocomposite films was dramatically enhanced by 103%, while the Young's modulus remarkably increased from 60 to 3540 MPa. Moreover, the storage modulus significantly improved by 34.5% was observed at loadings as low as 2.0 wt %. These enhancements were further investigated by means of differential scanning calorimetry and real time Fourier transform infrared spectra. A new perspective of balance was proposed to explain the improvement of those properties for the first time. At lower than 1.0 wt % loading, most of the g-C_3N_4 nanosheets were discrete in the SA matrix, resulting in improved thermal stability and mechanical properties; above 1.0 wt % and below 6.0 wt % content, the aggregation was present in SA host coupled with insufficient hydrogen bondings limiting the barrier for heat and leading to the earlier degradation and poor dispersion; at 6.0 wt % addition, the favorable balance was established with enhanced thermal and mechanical performances. However, the balance point of 2.0 wt % from dynamic mechanical analysis was due to combination of temperature and agglomeration. The work may contribute to a potential research approach for other nanocomposites.

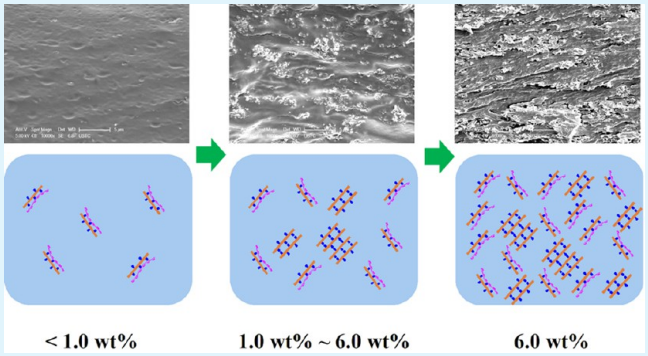

KEYWORDS: *sodium alginate, g-C_3N_4 nanosheets, mechanical property, thermal stability, hydrogen bonds, balance*

1. INTRODUCTION

Graphitic carbon nitride (g-C_3N_4), the most stable allotrope of carbon nitride with a stacked two-dimensional (2D) structure, has attracted increasing attention due to its fascinating properties such as thermal and chemical stability and optical and photoelectrochemical properties.[1,2] There are residual $-NH_2$ or $-NH$ groups presenting in g-C_3N_4, and the amount of these groups increases with the decrease of polycondensation degree,[3] where these groups can act as active sites for amide reaction or hydrogen bonding formation with other functional groups such as $-SH$, $-OH$, or $-COOH$. The g-C_3N_4 and its various derivatives have been widely studied in catalysts including photocatalysts and electrocatalysts,[4−10] hydrogen devices,[11,12] lithium ion storage,[13] optoelectronic equipment,[14,15] and bioimaging.[16] Moreover, g-C_3N_4-based polymer composites have also been investigated. Yan et al. revealed that g-C_3N_4-poly(3-hexylthiophene) (P3HT) composites contributed to enhancing the hydrogen production from water under

Received: October 12, 2013
Accepted: December 6, 2013
Published: December 6, 2013

Scheme 1. Schematic Representation of Pristine SA Film and Nanocomposite Film Formation

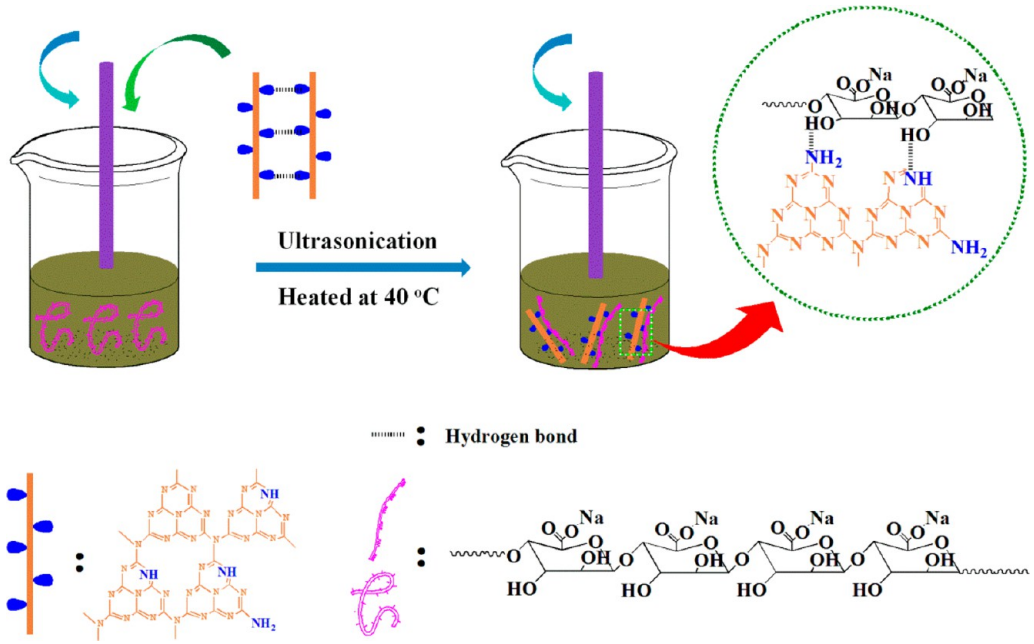

visible light.[12] Myllymaa et al. demonstrated that surface hydrophilicity of polypropylene (PP) was improved through the addition of silicon-doped carbon nitride (C_3N_4−Si) coating.[17] However, there are few previous reports on investigation into thermal stability and mechanical properties of polymer−g-C_3N_4 nanocomposites. Recently, Bao et al. reported that PVA nanocomposites exhibited enhanced mechanical strength by 66% and increased thermal stability by 32% with graphene of 0.8 and 1.6 wt %, respectively.[18] Those results revealed that the interfacial interactions among graphene and polymers and the physical barrier effect of graphene are the main reasons for these improvements. Given the fact that g-C_3N_4 is similar to graphene in structure, it is expected that combination of g-C_3N_4 and hydrophilic polymer can positively improve the thermal stability and mechanical properties of the polymer matrix. Compared to other 2D materials, such as graphene, montmorillonite (MMT), and layered double hydroxide (LDH), g-C_3N_4 is synthesized easily and rapidly, and especially inexpensively. Herein, novel g-C_3N_4-based biopolymer nanocomposites have been reported, which are different from those reported in previous works.

Sodium alginate (SA) is a water-soluble salt of alginic acid originating from a naturally occurring nontoxic polysaccharide found in all species of brown algae isolated from brown seaweeds.[19] There are a large number of hydroxyl groups (−OH) existing in the biopolymer electrolyte. Its applications have been widely reported including drug delivery,[20] biosensing devices,[21] and confection of dressings to treat exuding wounds[22] due to its excellent properties comprising biocompatibility, water absorption capacity, ability to form gels or films, and acceptable strength.[22−24] It has also been utilized for textile, paper, and food. However, some unsatisfactory properties such as poor mechanical strength, loss of structural integrity, and responsiveness to temperature limit its further applications.

Several strategies have been performed to enhance the thermal stability and mechanical properties of SA, most of which involve blending the alginate with a water-soluble polymer or some nanofillers. Typically, Ionita et al. revealed that the incorporation of 6.0 wt % graphene oxide (GO) into SA could obviously increase the tensile strength from 71 to 113 MPa and Young's modulus from 0.85 to 4.18 GPa, respectively, while the thermal stability was improved by ca. 30 °C.[25] Some improvements have been available, but a higher degree of enhancement is still necessary.

Scarcely any previous works on the integration of influencing factors for both thermal stability and mechanical properties have been reported. It is well-known that van der Waals interactions are weak interactions inferior in stress transfer compared with covalent or hydrogen bonds. On the basis of the above considerations and the fact that non-covalent bonds exist in g-C_3N_4-based SA nanocomposite films, hydrogen bonds are doubtlessly under the spotlight. There are three kinds of hydrogen bonds presenting in the nanocomposite films: (a) hydrogen bonds among SA molecular chains, (b) hydrogen bonds among g-C_3N_4 nanosheets, and (c) hydrogen bonds between g-C_3N_4 nanosheets and SA molecular chains. Whether hydrogen bond (a) or hydrogen bond (b), it is adverse to improvement in thermal and mechanical properties, resulting from both decreased intermolecular forces and emergence of agglomeration. However, hydrogen bond (c) results in a layered barrier effect to enhance thermal and mechanical properties due to the significant "tortuous path" effect of heat conduction, diffusion of gases and degradation products, and homogeneous distribution in polymer matrix.[26−30] There may be a balance between hydrogen bonds (c) and aggregation existing in the nanocomposite films. Thus, the aim of this work was to present a new sight to investigate the influence of g-C_3N_4 nanosheets on the thermal stability and mechanical properties of SA nanocomposite films. The possible mechanism was also discussed.

2. EXPERIMENTAL SECTION

2.1. Raw Materials. Urea and sodium alginate were purchased from Sinopharm Chemical Reagent Co., Ltd. (Shanghai, China). All reagents were used without further purification.

dx.doi.org/10.1021/am4044932 | ACS Appl. Mater. Interfaces 2014, 6, 429−437

2.2. Preparation of g-C_3N_4. The g-C_3N_4 nanosheets were synthesized by thermal pyrolysis.[31] In a typical process, after being dried at 80 °C, the urea was put in a crucible with a cover in air, then heated to 540 °C for 1 h, and further maintained at 540 °C for 5 h to complete the reaction. The as-synthesized product was a kind of light yellow powder.

2.3. Preparation of g-C_3N_4-Based SA Nanocomposite Films. The alginate solution was obtained by dissolving the sodium alginate in deionized water as 2.5% (w/w) solution under agitation at 40 °C. A 20 mg portion of g-C_3N_4 was dispersed in 20 mL of deionized water with sonication for 1 h to get a homogeneous distribution. Then, a mixture of the alginate solution and the g-C_3N_4 suspension was constantly stirred for 30 min under ultrasonication. Each solution was degassed and thrown onto a transparent flat film dish (10 × 20 cm^2) followed by being left undisturbed for 36 h at 40 °C, allowing formation of the nanocomposite film. The film was peeled off from the dish and labeled as SA-0.5 (0.5 wt % g-C_3N_4). The synthesis of nanocomposite films with other g-C_3N_4 contents (1.0, 2.0, 4.0, and 6.0 wt % corresponding to SA-1.0, SA-2.0, SA-4.0, and SA-6.0, respectively) was also performed on the basis of the strategy. The schematic representation for the formation of nanocomposite films is illustrated in Scheme 1. For comparison, the same method was used to produce pure SA film without g-C_3N_4.

2.4. Characterization. X-ray powder diffraction (XRD) patterns were performed by a Japan Rigaku Dmax X-ray diffractometer equipped with graphite monochromatized high-intensity Cu Kα radiation (λ = 1.54178 Å). The phase structure of g-C_3N_4 was observed in powdered state, while SA nanocomposite films were characterized using membrane samples.

Fourier transform infrared (FT-IR) spectroscopy (Nicolet 6700 FT-IR spectrophotometer) was employed to characterize the microstructure of as-synthesized products with a scanning range from 4000 to 400 cm^{-1} at room temperature.

Transmission electron microscopy (TEM) was provided by a JEOL 2010 instrument with an acceleration voltage of 200 kV. The morphology of g-C_3N_4 was observed by its dissolution in deionized water with ultrasonication and then dripped onto copper grids, while those of SA nanocomposite films were carried out in ultrathin state by using an Ultratome (Model MT-6000, Du Pont Company, USA) in liquid nitrogen before observation.

Thermogravimetric analysis (TGA) of the membrane samples was carried out by a Q5000 thermal analyzer (TA Co., USA) from 50 to 700 °C at a heating rate of 10 °C min^{-1} in air atmosphere with a flow rate of 100 mL min^{-1}.

The hydrogen bonding and crystallization behavior of SA nanocomposite films were investigated using a differential scanning calorimetry (DSC) Q2000 instrument (TA Instruments Inc., USA). Samples were heated from 0 to 200 °C at a rate of 10 °C min^{-1}, and then, the temperature was maintained at 200 °C for 10 min before being decreased from 200 to 0 °C at 10 °C min^{-1}. The temperature was kept at 0 °C for 10 min, and then, the heating−cooling cycle was performed again. The data for hydrogen bonding and crystallization behavior were obtained from the first heating and the second cooling, respectively.

Dynamic mechanical behavior was investigated by dynamic mechanical analysis (DMA) performed by a DMA Q800 instrument (TA Instruments Inc., USA) at a fixed frequency of 1 Hz and a temperature range from −90 to 110 °C at a heating rate of 5 °C min^{-1}. The storage modulus was plotted.

The tensile properties were measured according to GB13022-91 with a WD-20D electronic universal testing instrument (Changchun Intelligent Instrument Co. Ltd., China) at a crosshead speed of 2 mm min^{-1}. Nanocomposite membranes were cut into dumbbell-shaped pieces, and five parallel runs were performed for each sample to obtain an average.

The morphologies of the fracture surface from the nanocomposite films brittle failure used liquid nitrogen and sputter coated with a gold layer before observation were investigated by scanning electron microscopy (SEM) (AMRAY1000B, Beijing R&D Center of the Chinese Academy of Sciences, China).

Real time Fourier transform infrared (RTFT-IR) spectra were recorded using a Nicolet MAGNA-IR 750 spectrophotometer equipped with a heating device and a temperature controller. The samples were mixed with KBr powders and then pressed into a tablet, and then, they were placed in a ventilated oven. The temperature of the oven was raised at a heating rate of 10 °C min^{-1}. The dynamic FT-IR spectra were obtained during the thermal oxidative degradation process.

3. RESULTS AND DISCUSSION

3.1. Morphology and Structural Characterization of g-C_3N_4. The morphology of the as-obtained products was observed by TEM. The bare g-C_3N_4 shows a rippled 2D morphology and paper-like structure, which is similar to crumpled graphene (Figure 1).[32] During the pyrolysis process

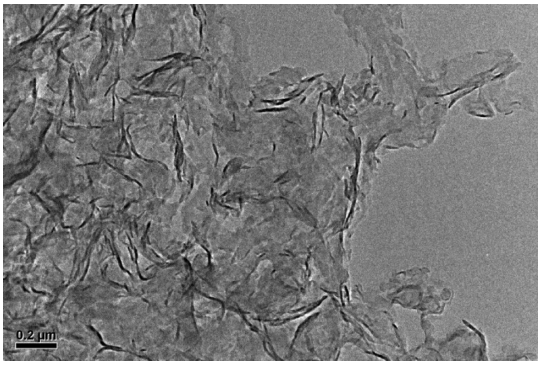

Figure 1. TEM micrograph of g-C_3N_4.

for g-C_3N_4 evolution, some gases, especially NH_3 and H_2O vapor, are generated from urea. These gases support the expansion of the stacking layers and facilitate the formation of g-C_3N_4 nanosheets with smaller thickness.

The FT-IR measurement was employed to dissect the microstructure of g-C_3N_4. The IR spectra are shown in Figure 1S (Supporting Information), revealing a typical molecular structure of g-C_3N_4. The absorption band located at ca. 810 cm^{-1} is assigned to vibration of the triazine ring. The bands at 1000−1800 cm^{-1} corresponded to stretching vibration of connected units such as C−N(−C)−C (full condensation) or C−NH−C (partial condensation). The broad peaks from 3000 to 3500 cm^{-1} are contributed by N−H stretching vibration and hydrogen bonding interactions.[32,33] These results demonstrate that g-C_3N_4 is endowed with intrinsic functional groups, such as −NH and $-NH_2$, acting as potential anchoring sites for metal ions or coupling with −OH and −COOH groups.

3.2. Structural Characterization of g-C_3N_4-Based SA Nanocomposite Films. Figure 2 depicts the XRD patterns of g-C_3N_4, SA, and the nanocomposite films. The related data are recorded in Table 1S (Supporting Information). It is observed from both Figure 2 and Table 1S (Supporting Information) that the strongest diffraction peak at 2θ = 27.72° is attributed to the stacking of the conjugated aromatic system, which is consistent with the reported g-C_3N_4.[34] The in-planar repeating unit with a period of 0.671 nm is clearly observed at 13.18°. In the case of virgin SA film, the broad peak at 2θ = 13.34° with an average intermolecular distance of 6.66 Å reveals a rather amorphous structure.[35] Two diffraction peaks at 13.4 and 23−28° are obviously observed for all the nanocomposite films, especially for SA-6.0, which are assigned to both SA and g-C_3N_4. The diffraction angle characteristic of g-C_3N_4 is shifted

dx.doi.org/10.1021/am4044932 | ACS Appl. Mater. Interfaces 2014, 6, 429−437

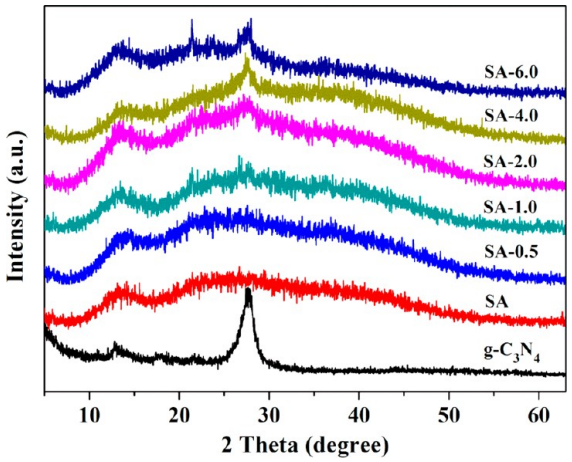

Figure 2. XRD curves of g-C_3N_4 and SA nanocomposite films with different contents of g-C_3N_4.

towards a lower value (Table 1S, Supporting Information), and its interlayer spacing increases from 3.31 Å for pristine g-C_3N_4 to 3.84 Å for SA-0.5, indicating the formation of intercalated structures. It is worth noting that the migratory amplitude of the peak at 2θ = 27.72° wears off with the increase of g-C_3N_4 content, implying that the aggregation happens at high loadings. However, the structure of SA is not significantly affected by the introduction of g-C_3N_4, suggesting that there are mainly physical interactions between g-C_3N_4 and SA.[36] Owing to the presence of −OH from SA and $-NH_2$ or −NH from g-C_3N_4, it is a conclusive result that the hydrogen bonds are existent between SA chains and g-C_3N_4 nanosheets.

The interactions between g-C_3N_4 nanosheets and SA chains were investigated by FT-IR measurements. Figure 3 exhibits

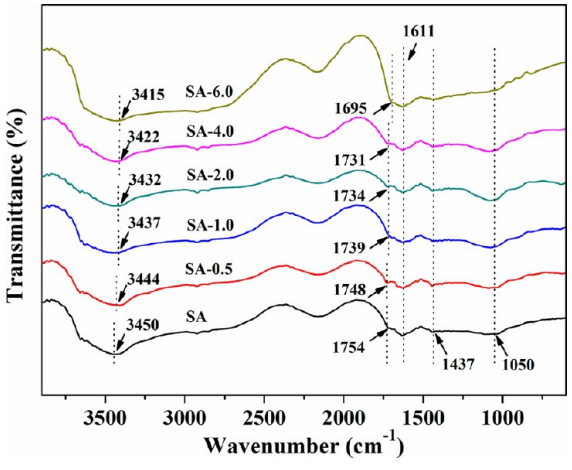

Figure 3. FT-IR spectra of SA nanocomposite films with different loading levels.

characteristic absorption bands of pure SA film and the nanocomposite films. For neat SA film, the peak at 3450 cm^{-1} is associated with O−H stretching vibration; the bands at 1611 and 1437 cm^{-1} correspond to symmetric and asymmetric COO^- stretching vibration of the carboxylate salt group; and the peak at 1050 cm^{-1} is assigned to the stretching vibration of C−O−C groups.[37] In addition, a shoulder peak at around 1754 cm^{-1} is attributed to the −COOH group due to the partial hydrolysis of carboxylate salt. These −OH or −COOH groups act as active sites for the interaction with the $-NH_2$ or −NH groups of g-C_3N_4. From the nanocomposite films, the peaks at 3450 and 1754 cm^{-1} are broadened and shifted to lower wavenumber, indicative of the interaction of SA chains and g-C_3N_4 nanosheets through intermolecular hydrogen bonds.[25,38] Moreover, the shifts are clearly found in magnified IR spectra (Figure 2S, Supporting Information). The hydrogen bonding interactions between SA chains and g-C_3N_4 nanosheets may induce good interfacial adhesion at the interface SA/g-C_3N_4 and result in enhanced thermal stability and mechanical performances.

3.3. Thermal Stability and Hydrogen Bonding Behavior of g-C_3N_4-Based SA Nanocomposite Films.

The thermal stability of g-C_3N_4-based SA nanocomposite films was investigated by TGA. The corresponding curves are shown in Figure 4, and the data are summarized in Table 2S (Supporting Information). SA tends to adsorb water due to the existence of hydroxyl and carboxyl groups in its molecules. Three stages are visible in the process of thermal weight loss. The first stage terminated by 200 °C is caused by the traces of moisture present. $T_{-5\%}$ corresponding to the temperature at 5 wt % mass loss is obtained at 133.2 °C. The decomposition of SA containing the hydroxyl and carboxyl groups and polymer chains is observed between 200 and 580 °C.[39] The initial decomposition and half degradation in this stage are evaluated by $T_{-10\%}$ and $T_{-50\%}$, respectively. The third stage ranging from 580 to 700 °C is attributed to the thermal-oxidized degradation of the SA backbone, leading to the residual formation. In the case of SA nanocomposite films, higher $T_{-5\%}$ is available except for SA-0.5, which indicates that more moisture is existent in the film due to the incomplete drying. Furthermore, $T_{-50\%}$ for all the SA nanocomposite films is increased (316.8 °C for SA-0.5) compared with that of pure SA film (243.7 °C), especially for SA-6.0 (361.9 °C). The trend, accompanied by those of $T_{-5\%}$ and $T_{-10\%}$, suggests that more hydrogen bonds associated with the physical barrier of g-C_3N_4 lamellar structure for the heat conduction are generated from increasing content except that of SA-1.0, revealing that balance between hydrogen bonds (c) and agglomeration is worthy of consideration. Below 1.0 wt %, most of the g-C_3N_4 nanosheets are discrete in the SA matrix; at 1.0−4.0 wt %, the aggregation is present in SA matrix accompanied with insufficient hydrogen bonds limiting the barrier for heat and leading to the earlier degradation; at 6.0 wt %, the favorable balance is established. However, in the third stage, the earlier degradation occurs in SA-6.0 due to the relative decrease of hydrogen bonds, resulting in the destruction of the balance. Nonetheless, all the SA nanocomposite films have the higher residues with gradual decrease as g-C_3N_4 content increases compared to native SA film. Owing to the almost complete decomposition of g-C_3N_4 at 700 °C, the higher residues are generated from the catalytic charring effect of isolated g-C_3N_4 nanosheets. On the basis of the above results, it is obvious that introduction of g-C_3N_4 nanosheets into the matrix is beneficial to significantly enhance thermal stability by the physical barrier effect for the heat conduction during decomposition.

DSC was performed to investigate the hydrogen bonding and crystallization behavior of SA nanocomposite films. The thermodynamic equation is

$$\Delta H = \Delta U + \Delta(PV) \quad (1)$$

where ΔH, ΔU, P, and V mean enthalpy change, internal energy change, pressure, and volume, respectively. Given the

dx.doi.org/10.1021/am4044932 | ACS Appl. Mater. Interfaces 2014, 6, 429−437

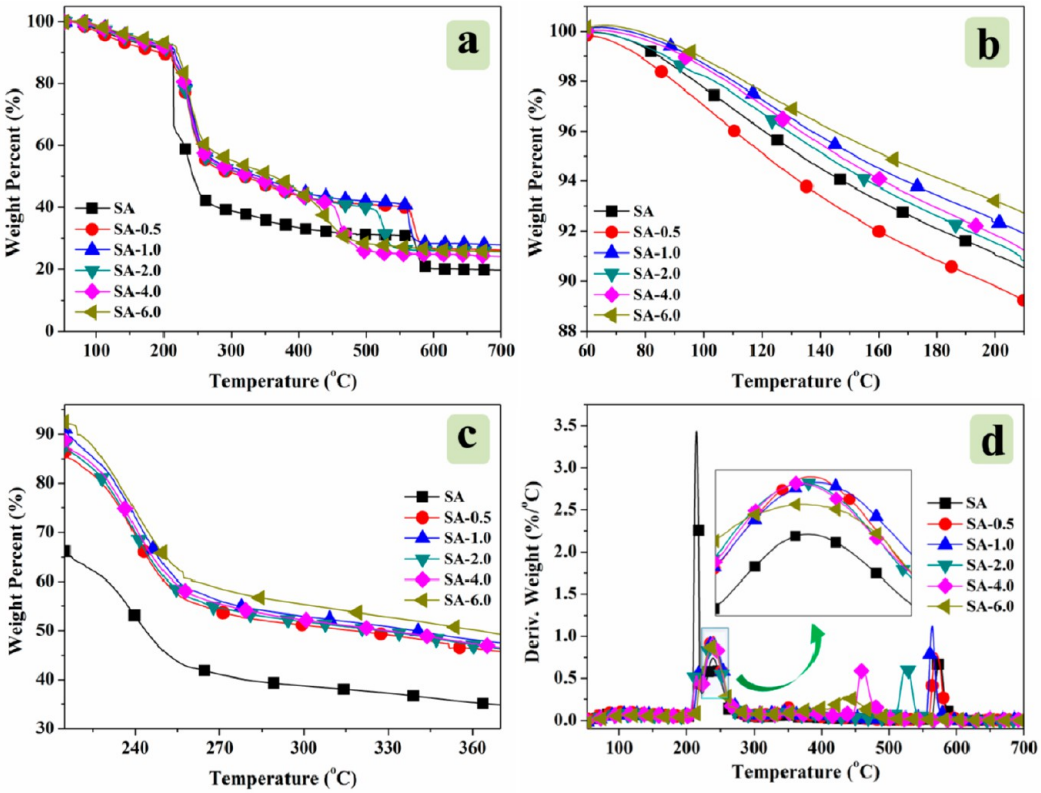

Figure 4. TGA (a) and DTG (d) curves of g-C_3N_4-based SA nanocomposite films obtained at a heating rate of 10 °C min^{-1} in air atmosphere; parts b and c present the different magnified sections of part a.

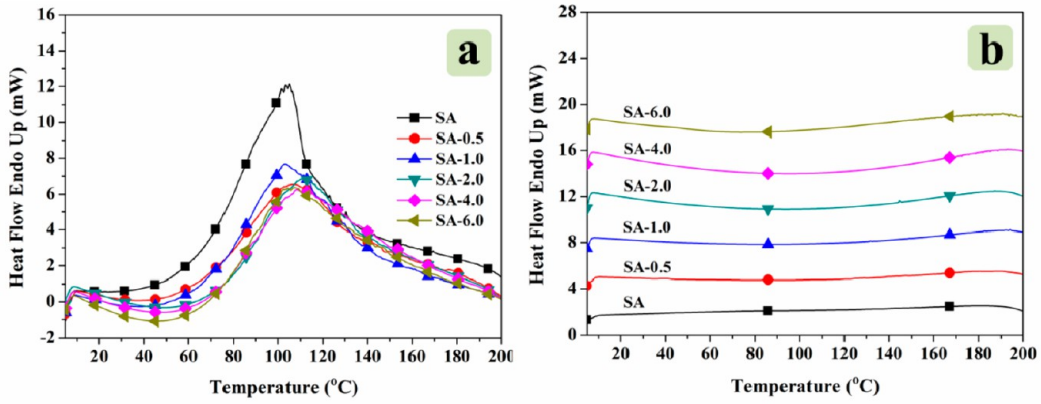

Figure 5. DSC curves of (a) enthalpy values and (b) crystallization behavior of various SA nanocomposite films.

matter of the constant pressure, the evolutive formula is depicted as follows:

$$\Delta H = \Delta U + P\Delta V \quad (2)$$

where ΔH represents the endothermic process. Hydrogen bonds with weak energy of 25−40 kJ/mol are responsive to temperature. The destruction of hydrogen bonds with the increase of temperature is necessary for absorbing heat from the outside. Herein, enthalpy is used as an important parameter to investigate the hydrogen bondings. Figure 5a and Table 3S (Supporting Information) are the DSC curves and enthalpy values of SA nanocomposite films, respectively, showing that ΔH values are increased gradually with the increment of g-C_3N_4 content for all the SA nanocomposite films, which is indicative of increased agglomeration. These values of SA nanocomposite films are low with respect to that of native SA film, revealing the existence of monolayer demonstrated by similar works.[40] This is consistent with the TGA results. The crystallization behavior of SA nanocomposite films is studied, and the results are depicted in Figure 5b. The constantly broadened exothermic peaks of these nanocomposite films appear with the increase of g-C_3N_4 content, suggesting that the crystallization is induced by hydrogen bonds (c) but inhibited by aggregation.[41] Orientation of the nanosheets arised from hydrogen bonds (c) may further enhance barrier effect perpendicular to their alignment.[42] The results from Figure 5 demonstrate that hydrogen bonds (c) and agglomeration coexist in SA nanocomposite films.

3.4. Thermal Oxidative Behavior of g-C_3N_4-Based SA Nanocomposite Films. RTFT-IR was employed to explore

dx.doi.org/10.1021/am4044932 | ACS Appl. Mater. Interfaces 2014, 6, 429−437

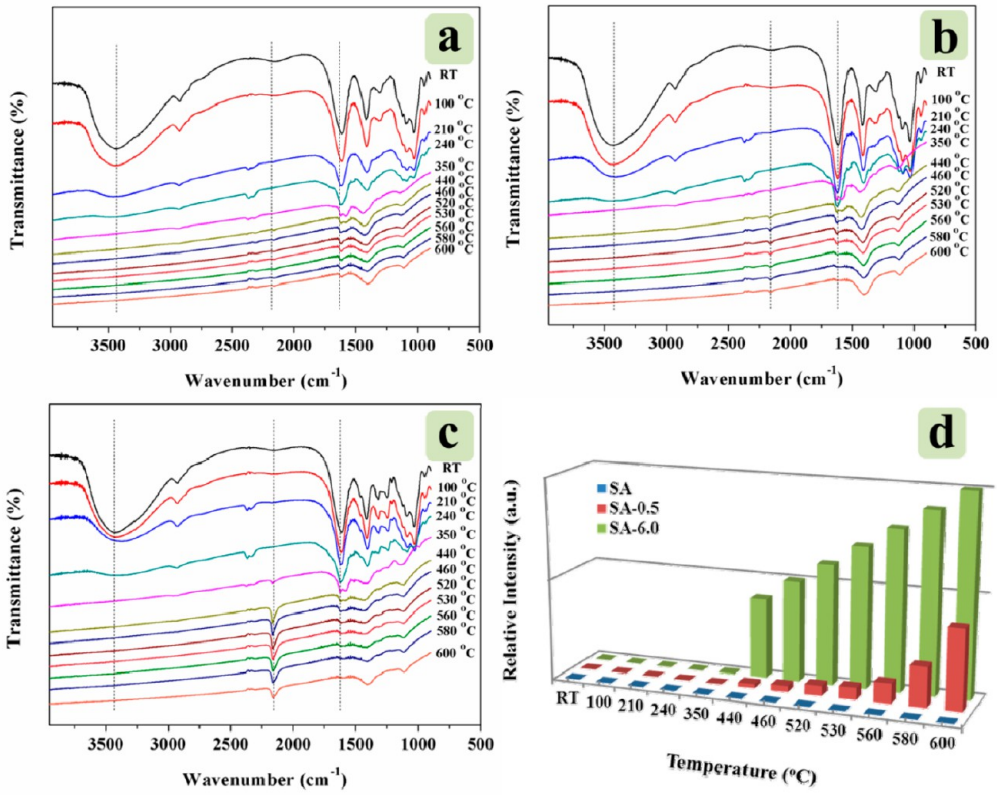

Figure 6. RTFT-IR spectra of SA and its nanocomposite films at different pyrolysis temperatures: (a) SA; (b) SA-0.5; (c) SA-6.0; (d) $I_{2154cm^{-1}}/I_{1617cm^{-1}}$ of SA nanocomposite films vs temperature.

the details of thermal oxidative behavior of SA nanocomposite films. Figure 6 shows the RTFT-IR spectra and relative intensity ($I_{2154cm^{-1}}/I_{1617cm^{-1}}$) change with different temperatures of SA nanocomposite films. It is evident that all the hydrogen bonds are terminated by 240 °C and gradually increased interaction from hydrogen bonds is observed in SA nanocomposite films with growing loadings (Figure 6a, b, and c). The peaks at 2154 and 1617 cm^{-1} are attributed to the formation of NH_2^+, further confirming that the hydrogen bonds have been destroyed. Moreover, the pyrolysis route has also been obtained from both 2154 and 1617 cm^{-1} due to the incorporation of g-C_3N_4 nanosheets. Figure 6d is a spectrum of relative intensity ratio ($I_{2154cm^{-1}}/I_{1617cm^{-1}}$) versus temperature, indicating that the transformation is thorough in high loading levels. These results provide strong evidence that poor thermal stability of SA-6.0 at high temperature is ascribed to hydrogen bonds (c) being broken.

3.5. The Mechanical Performance of g-C_3N_4-Based SA Nanocomposite Films. The mechanical behavior of the nanocomposite films containing 0.5−6.0 wt % g-C_3N_4 is depicted in Figure 7, and the related data are given in Table 4S (Supporting Information). As can be seen from Figure 7 and Table 4S (Supporting Information), the ever-increasing tensile strength occurring in all the nanocomposite films is originated from the increased g-C_3N_4 content, especially the maximal increase by 103% for SA-6.0. Increase in elongation at break is observed for SA-0.5 and SA-1.0 relative to pristine SA film. The former results from the incomplete drying, demonstrated by the TGA results and further confirmed according to the value of Young's modulus, while the latter is ascribed to the existence of insular g-C_3N_4 nanosheets in SA matrix without aggregation. However, its decrease for other SA nanocomposite films may

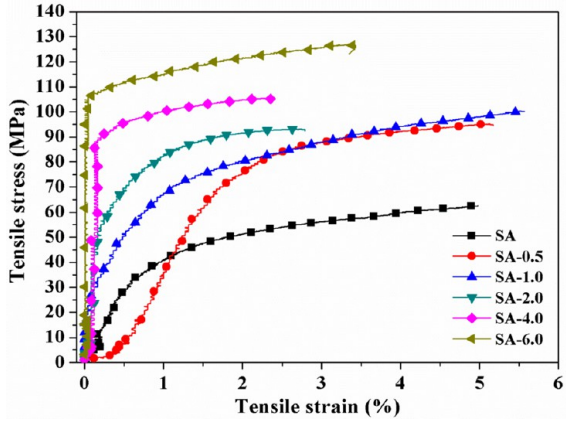

Figure 7. The typical stress−strain curves of SA and its nanocomposite films.

be attributed to the presence of some stacks in g-C_3N_4 nanosheets. The data from Table 4S (Supporting Information) exhibit that the modulus increases from 60.1 ± 10.2 (for neat SA) to 3539.6 ± 10.2 MPa. The maximum modulus value obtained from 6.0 wt % g-C_3N_4 provides more stiffness to the materials, suggesting that it is dependent on the loading level of the nanosheets. The improvement in Young's modulus can be explained as increased hydrogen bondings between the SA chains and g-C_3N_4 nanosheets. Additionally, it reveals that hydrogen bonding (c) is prominent before establishing the balance.

On the basis of the discussion aforementioned, it is inferred that the balance between hydrogen bonds (c) and aggregation is existent in SA nanocomposite films. Both thermal stability

dx.doi.org/10.1021/am4044932 | ACS Appl. Mater. Interfaces 2014, 6, 429−437

Scheme 2. The Possible Mechanism for Enhanced Properties of SA Nanocomposite Films with Different g-C_3N_4 Contents[a]

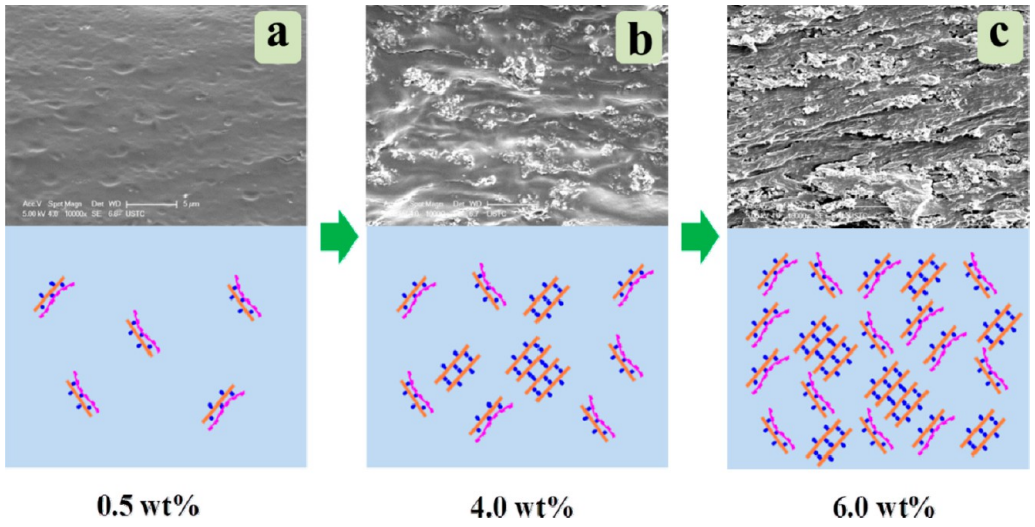

[a]The content of g-C_3N_4 is increased from a to c.

and mechanical properties are improved at low loadings as 1.0 wt %, where most of the g-C_3N_4 nanosheets were distributed in the SA matrix with island-like state; they worsened at 1.0−4.0 wt % due to the aggregation accompanied by insufficient hydrogen bondings limiting the barrier for heat and giving rise to the earlier degradation and poor dispersion; they significantly enhanced at 6.0 wt % upon the establishment of balance. The proposed mechanism for these improved properties is depicted in Scheme 2.

3.6. Dynamic Mechanical Analysis of g-C_3N_4-Based SA Nanocomposite Films. To investigate the correlation between mechanical performance and temperature, DMA was carried out in this work. The curves of storage modulus as a function of temperature are plotted in Figure 8. The storage

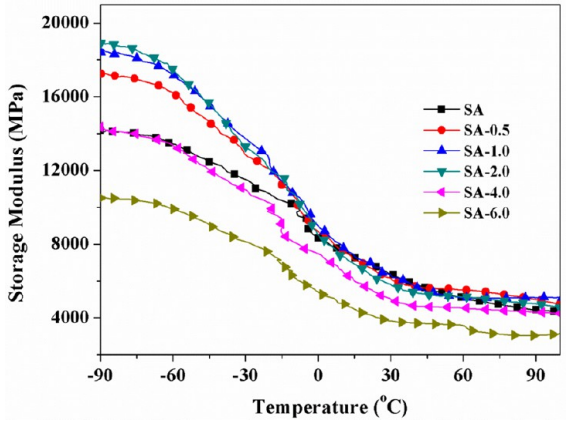

Figure 8. DMA curves of SA nanocomposite films as a function of SA/g-C_3N_4 contents.

modulus is a measure of the stiffness, and the nanocomposite films exhibit remarkable enhancement in storage modulus except for SA-4.0 and SA-6.0 resulting from the serious aggregation. The SA-2.0 exhibits a maximum increase by 34.5% compared with neat SA at −90 °C. The results indicate that the balance between aggregation and hydrogen bonding (c) is established at 2.0 wt % content. The reinforcement effect is sensitive to the g-C_3N_4 loading at less than 2.0 wt %, due to the stronger interfacial interactions in SA/g-C_3N_4, but is deteriorated above 2.0 wt % because of the aggregation. Noteworthily, the different balance points obtained from tensile and DMA measurements may be attributed to the fact that SA itself is responsive to temperature. Low temperature leads to stronger hydrogen bonding interaction among SA chains. The presence of isolated g-C_3N_4 nanosheets strengthens the interaction, while aggregation worsens it. The balance established at 2.0 wt % reveals the combining effect of both temperature and loading level.

3.7. The Morphology of g-C_3N_4-Based SA Nanocomposite Films. SEM was employed to determine the morphology of nanocomposite films. Figure 9 displays the images of SA nanocomposite films. It is clearly found from the fracture surface micrograph (Figure 9a) that the SA film has a cracked surface due to irradiation of high energy electron beams. Both SA-0.5 and SA-1.0 show a homogeneous morphology (Figure 9b and c), indicating the presence of hydrogen bonds associated with a physical barrier effect. However, there is a serious crack in SA-1.0, resulting from the irradiation of high energy electron beams. The agglomeration, as shown in Figure 9d, e, and f, happens with content exceeding 1.0 wt %. Moreover, the distribution of g-C_3N_4 nanosheets in SA matrix is also visible in Figure 10. The element mapping exhibits the insular dispersion of N element in specific portion (Figure 10a and b) of SA-0.5 and SA-1.0 selected for the mapping studies due to low loading of g-C_3N_4 nanosheets. The aggregation is presented in Figure 10c corresponding to SA-4.0. For SA-6.0, it is not obvious that the aggregation can be observed due to g-C_3N_4 nanosheets overspreading completely. However, in the case of all the nanocomposite films, it is evident that C, O, and Na elements are uniformly dispersed in SA matrix (Figure 3S, Supporting Information). To further evaluate the distribution of g-C_3N_4 nanosheets in SA host, an ultrathin section is available to obtain the microstructure. Figure 11 shows the TEM observations of the ultrathin sections of the nanocomposite films, showing that g-C_3N_4 nanosheets indeed exist in island-like morphology and partially exfoliated into individual nanosheets (Figure 11a and b). Unfortunately, high loadings lead to irreversible aggregation. From the nanocomposite film images (Figure 11c and d), noticeable

dx.doi.org/10.1021/am4044932 | ACS Appl. Mater. Interfaces 2014, 6, 429−437

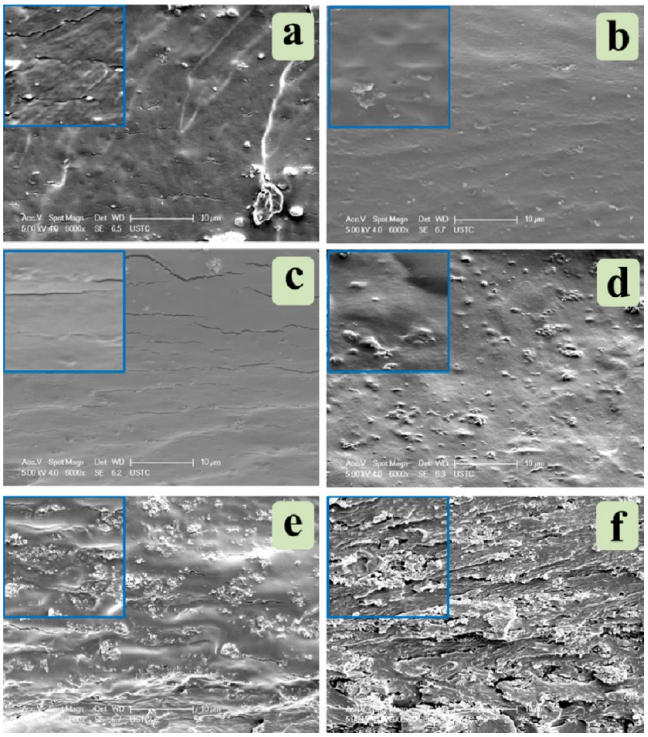

Figure 9. SEM fracture surface images of SA nanocomposite films: (a) SA; (b) SA-0.5; (c) SA-1.0; (d) SA-2.0; (e) SA-4.0; (f) SA-6.0. The insets present the corresponding magnification images.

agglomeration and homogeneous distribution are coexistent in the SA matrix. These results from SEM and TEM images are accordant with TGA and tensile results, further demonstrating the establishment of the balance between hydrogen bonds (c) and agglomeration in SA nanocomposite films.

4. CONCLUSIONS

In this work, g-C_3N_4-based SA nanocomposite films have been prepared by the casting technique. Thermal stability of all the nanocomposite films was enhanced significantly, including $T_{-10\%}$ increased by 29.1 °C and $T_{-50\%}$ improved by 118.2 °C. Introduction of 6.0 wt % g-C_3N_4 led to the tensile strength of SA nanocomposite films being maximally reinforced by 103% and the Young's modulus increasing from 60 to 3540 MPa. Moreover, the storage modulus enhanced by 34.5% was observed at loadings as low as 2.0 wt %. A new sight was developed to investigate the nanocomposite films. The hydrogen bonding interactions between g-C_3N_4 nanosheets and SA host led to remarkable enhancements in thermal stability and mechanical properties. For these improvements, the balance between hydrogen bonds (c) and aggregation was proposed for the first time. The hydrogen bondings (c) resulted in enhanced thermal stability and mechanical performances, which was attributed to a favorable barrier effect. Lower than 1.0 wt %, most g-C_3N_4 nanosheets were isolated in the SA matrix, leading to improved thermal stability and mechanical properties; at 1.0−4.0 wt %, the aggregation limited the barrier for heat and led to the earlier degradation and poor dispersion; at 6.0 wt %, the improved thermal and mechanical performances were obtained from the balance. However, the balance was established in 2.0 wt % content for dynamic mechanical behavior of SA nanocomposite films. The modulus was enhanced below 2.0 wt % arising from hydrogen bonds (c),

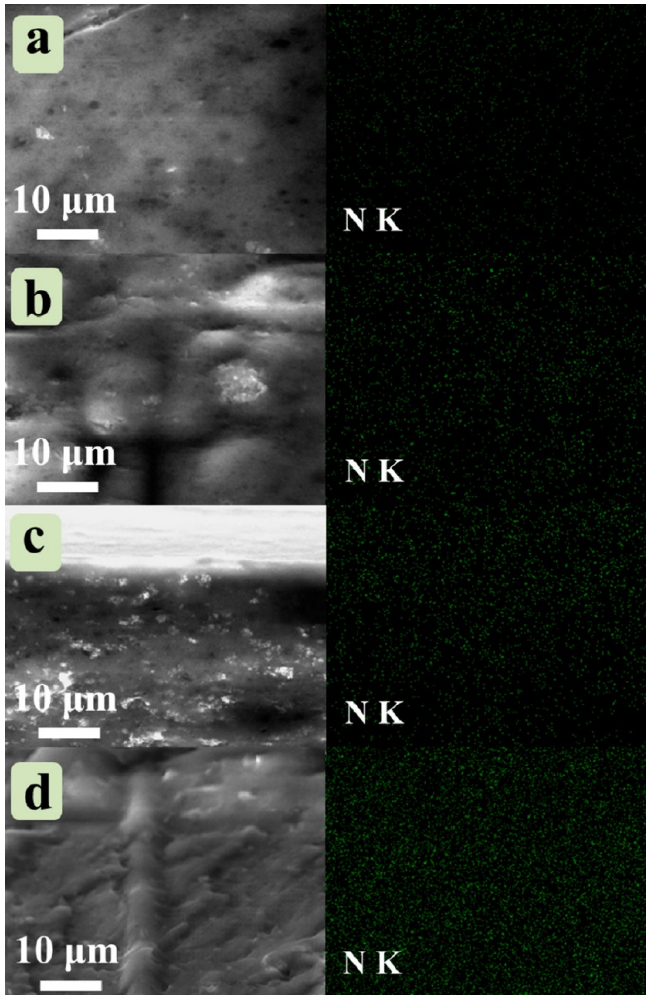

Figure 10. SEM fracture surface mapping of SA nanocomposite films: (a) SA-0.5; (b) SA-1.0; (c) SA-4.0; (d) SA-6.0.

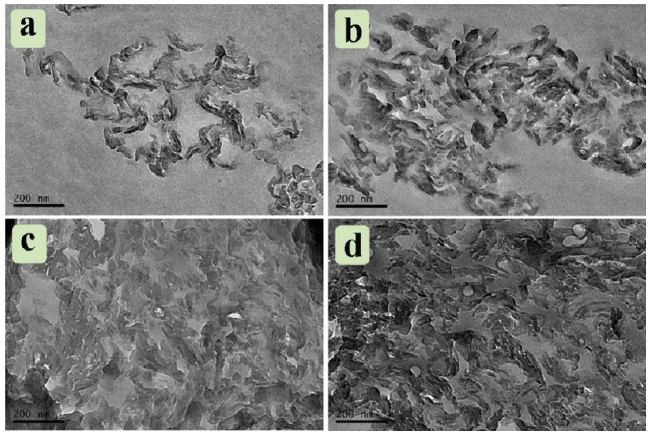

Figure 11. TEM ultrathin section images of SA nanocomposite films: (a) SA-0.5; (b) SA-1.0; (c) SA-4.0; (d) SA-6.0.

while it was worsened above 2.0 wt % due to the aggregation, which was originated from combination of temperature and agglomeration. In summary, the results for g-C_3N_4-based SA nanocomposite films indicate that the wrinkled nanosheets afford better enhancement in thermal stability and mechanical properties compared to GO at exceptionally low loadings. These −NH and $-NH_2$ groups on the g-C_3N_4 nanosheets may

dx.doi.org/10.1021/am4044932 | ACS Appl. Mater. Interfaces 2014, 6, 429−437

be well suited to form nanocomposites with other hydrophilic polymers such as polyvinyl alcohol (PVA) and chitosan (CTS), resulting in intimate nanosheet−polymer interactions essential to thermal and mechanical improvements. However, it is not suitable for hydrophobic polymers because of its high chemical stability. For example, it is insoluble in almost all organic solvents such as *N*,*N*-dimethylformamide (DMF), tetrahydrofuran (THF), acetone, pyridine, $CHCl_3$, etc., which can act as excellent dissolvants for the kind of polymer. Therefore, various strategies to obtain good dispersion are of great necessity. Importantly, the application of g-C_3N_4-based SA nanocomposite films is to be investigated in our future work.

■ ASSOCIATED CONTENT

Supporting Information

Tables showing the related XRD data, TGA data, related DSC data, and corresponding mechanical properties of SA and its nanocomposite films. Figures showing FT-IR spectroscopy of g-C_3N_4, the magnified FT-IR spectra of SA and its nanocomposite films, and SEM fracture surface mapping of SA nanocomposite films. This material is available free of charge via the Internet at http://pubs.acs.org.

■ AUTHOR INFORMATION

Corresponding Authors

*Phone: +86-551-3601288. Fax: +86-551-3601669. E-mail: zgui@ustc.edu.cn.

*Phone: +86-551-3601664. Fax: +86-551-3601664. E-mail: yuanhu@ustc.edu.cn.

Notes

The authors declare no competing financial interest.

■ ACKNOWLEDGMENTS

This work was financially supported by the National Natural Science Foundation of China (No. 21071138) and National Basic Research Program of China (973 Program) (No. 2012CB922002). Moreover, the authors thank Mr Yonglong Zhuang for assisting with the TEM measurement.

■ REFERENCES

(1) Wang, X. C.; Maeda, K.; Thomas, A.; Takanabe, K.; Xin, G.; Carisson, J. M.; Domen, K.; Antonietti, M. *Nat. Mater.* **2009**, *8*, 76−80.
(2) Wang, Y.; Wang, X. C.; Antonietti, M. *Angew. Chem., Int. Ed.* **2012**, *51*, 68−89.
(3) Bojdys, M. J.; Müller, J. O.; Antonietti, M.; Thomas, A. *Chem.—Eur. J.* **2008**, *14*, 8177−8182.
(4) Wang, X. C.; Blechert, S.; Antonietti, M. *ACS Catal.* **2012**, *2*, 1596−1606.
(5) Niu, P.; Liu, G.; Cheng, H. M. *J. Phys. Chem. C* **2012**, *116*, 11013−11018.
(6) Noto, V. D.; Negro, E.; Polizzi, S.; Riello, P.; Atanassov, P. *Appl. Catal., B* **2012**, *111−112*, 185−199.
(7) Wang, Y. B.; Hong, J. D.; Zhang, W.; Xu, R. *Catal. Sci. Technol.* **2013**, *3*, 1703−1711.
(8) Zhang, J. S.; Grzelczak, M.; Hou, Y. D.; Maeda, K.; Domen, K.; Fu, X. Z.; Antonietti, M.; Wang, X. C. *Chem. Sci.* **2012**, *3*, 443−446.
(9) Zhu, J. J.; Wei, Y. C.; Chen, W. K.; Zhao, Z.; Thomas, A. *Chem. Commun.* **2010**, *46*, 6965−6967.
(10) Yan, H. J.; Chen, Y.; Xu, S. M. *Int. J. Hydrogen Energy* **2012**, *37*, 125−133.
(11) Lin, Z. Z.; Wang, X. C. *Angew. Chem., Int. Ed.* **2013**, *52*, 1735−1738.
(12) Yan, H. J.; Huang, Y. *Chem. Commun.* **2011**, *47*, 4168−4170.
(13) Fang, Y.; Lv, Y. Y.; Che, R. C.; Wu, H. Y.; Zhang, X. H.; Gu, D.; Zheng, G. F.; Zhao, D. Y. *J. Am. Chem. Soc.* **2013**, *135*, 1524−1530.
(14) Zhang, Y. J.; Mori, T.; Niu, L.; Ye, J. H. *Energy Environ. Sci.* **2011**, *4*, 4517−4521.
(15) Zhang, Y. J.; Mori, T.; Ye, J. H.; Antonietti, M. *J. Am. Chem. Soc.* **2010**, *132*, 6294−6295.
(16) Zhang, X. D.; Xie, X.; Wang, H.; Zhang, J. J.; Pan, B. C.; Xie, Y. *J. Am. Chem. Soc.* **2013**, *135*, 18−21.
(17) Myllymaa, K.; Myllymaa, S.; Korhonen, H.; Lammi, M. J.; Saarenpää, H.; Suvanto, M.; Pakkanen, T. A.; Tiitu, V.; Lappalainen, R. *J. Mater. Sci.: Mater Med.* **2009**, *20*, 2337−2347.
(18) Bao, C. L.; Guo, Y. Q.; Song, L.; Hu, Y. *J. Mater. Chem.* **2011**, *21*, 13942−13950.
(19) Wong, T. Y.; Preston, L. A.; Schiller, N. L. *Annu. Rev. Microbiol.* **2000**, *54*, 289−340.
(20) Gazori, T.; Khoshayand, M. R.; Azizi, E.; Yazdizade, P.; Nomani, A.; Haririan, I. *Carbohydr. Polym.* **2009**, *77*, 599−606.
(21) Kauffman, J. S.; Ellerbrock, B. M.; Stevens, K. A.; Brown, P. J.; Pennington, W. T.; Hanks, T. W. *ACS Appl. Mater. Interfaces* **2009**, *1*, 1287−1291.
(22) Qin, Y. *Polym. Adv. Technol.* **2008**, *19*, 6−14.
(23) Becker, T. A.; Kipke, D. R.; Brandon, T. *J. Biomed. Mater. Res.* **2001**, *54*, 76−86.
(24) Majima, T.; Funakosi, T.; Iwasaki, N.; Yamane, S. T.; Harada, K.; Nonaka, S.; Minami, A.; Nishimura, S. *J. Orthop. Sci.* **2005**, *10*, 302−307.
(25) Ionita, M.; Pandele, M. A.; Iovu, H. *Carbohydr. Polym.* **2013**, *94*, 339−344.
(26) Bao, C. L.; Song, L.; Wilkie, C. A.; Yuan, B. H.; Guo, Y. Q.; Hu, Y.; Gong, X. L. *J. Mater. Chem.* **2012**, *22*, 16399−16406.
(27) Bao, C. L.; Song, L.; Xing, W. Y.; Yuan, B. H.; Wilkie, C. A.; Huang, J. L.; Guo, Y. Q.; Hu, Y. *J. Mater. Chem.* **2012**, *22*, 6088−6096.
(28) Huang, G. B.; Gao, J. R.; Wang, X.; Liang, H. D.; Ge, C. H. *Mater. Lett.* **2012**, *66*, 187−189.
(29) Wang, X.; Song, L.; Yang, H. Y.; Xing, W. Y.; Lu, H. D.; Hu, Y. *J. Mater. Chem.* **2012**, *22*, 3426−3431.
(30) Shi, Y. Q.; Qian, X. D.; Zhou, K. Q.; Tang, Q. B.; Jiang, S. H.; Wang, B. B.; Wang, B.; Yu, B.; Hu, Y.; Yuen, R. K. K. *Ind. Eng. Chem. Res.* **2013**, *52*, 13654−13660.
(31) Shi, Y. Q.; Jiang, S. H.; Zhou, K. Q.; Wang, B. B.; Wang, B.; Gui, Z.; Hu, Y.; Yuen, R. K. K. *RSC Adv.* **2013**, DOI: 10.1039/C3RA44256J.
(32) Lotsch, B. V.; Doblinger, M.; Sehnert, J.; Seyfarth, L.; Senker, J.; Oeckler, O.; Schnick, W. *Chem.—Eur. J.* **2007**, *13*, 4969−4980.
(33) Qiu, Y.; Gao, L. *Chem. Commun.* **2003**, *0*, 2378−2379.
(34) Wang, X. C.; Maeda, K.; Chen, X. F.; Takanabe, K.; Domen, K.; Hou, Y. D.; Fu, X. Z.; Antonietti, M. *J. Am. Chem. Soc.* **2009**, *131*, 1680−1681.
(35) Kim, S. G.; Lim, G. T.; Jegal, J.; Lee, K. J. *J. Membr. Sci.* **2000**, *174*, 1−15.
(36) Han, D. L.; Yan, L. F.; Chen, W. F.; Li, W. *Carbohydr. Polym.* **2011**, *83*, 653−658.
(37) Sartori, C.; Finch, D. S.; Ralph, B.; Gilding, K. *Polymer* **1997**, *38*, 43−51.
(38) Salavagione, H. J.; Martinez, G.; Gomez, M. A. *J. Mater. Chem.* **2009**, *19*, 5027−5032.
(39) Rani, P.; Mishra, S.; Sen, G. *Carbohydr. Polym.* **2013**, *91*, 686−692.
(40) Osman, M. A.; Rupp, J. E. P. *Macromol. Rapid Commun.* **2005**, *26*, 880−884.
(41) Gao, Y.; Choudhury, N. R.; Dutta, N. K. *J. Appl. Polym. Sci.* **2010**, *117*, 3395−3405.
(42) Paul, D. R.; Robeson, L. M. *Polymer* **2008**, *49*, 3187−204.